Digital in-line holography to explore saliva aerosolization mechanisms in speech

Ashley Nord, Patrice Dosset, Pierre Slangen, Manouk Abkarian

To cite this version:

Ashley Nord, Patrice Dosset, Pierre Slangen, Manouk Abkarian. Digital in-line holography to explore saliva aerosolization mechanisms in speech. Journal of Aerosol Science, 2024, 175, pp.106282. 10.1016/j.jaerosci.2023.106282 . hal-04266348

HAL Id: hal-04266348
https://imt-mines-ales.hal.science/hal-04266348v1

Journal of Aerosol Science 175 (2024) 106282

Contents lists available at ScienceDirect

Journal of Aerosol Science

journal homepage: www.elsevier.com/locate/jaerosci

Digital in-line holography to explore saliva aerosolization mechanisms in speech

Ashley L. Nord [a,1], Patrice Dosset [a,1], Pierre Slangen [b], Manouk Abkarian [a,*]

[a] *Centre de Biologie Structurale, Université de Montpellier, CNRS, INSERM, Montpellier, France*
[b] *EuroMov Digital Health in Motion, Univ Montpellier, IMT Mines Ales, Ales, France*

ARTICLE INFO

Editor: Dr. Chris Hogan

Keywords:
Speech
Saliva
Aerosolization
Filament
Plosives

ABSTRACT

Phonation produces aerosols, and speech has proven to be a pernicious, invisible, yet potent viral transmission route among asymptomatic individuals in the COVID-19 pandemic. To develop comprehensive mitigation strategies and mechanisms to control transmission, it is crucial to measure both the amount of aerosols produced by a speaking individual and the associated atomization processes. However, these biological emissions are hard to characterize since they are intermittent, faint, range drastically in size between 1 and 1000 μm, and form and travel rapidly, with speeds of a few to tens of meters per second. Here, we present digital in-line holography (DIH) as a lens-less and powerful tool to overcome many of these experimental challenges. Focusing on speech-induced aerosolization, we demonstrate the capacity of DIH to image the rapid formation, elongation, and deformation of saliva filaments in three dimensions and directly at the mouth of a speaking individual. The size of both the filaments and the subsequent aerosolized droplets are accessible over a field of view spanning several centimeters cubed. We quantify the droplets produced by distinct plosive consonants (/p/ and/t/) and we observe how filaments destabilize with a characteristic whipping dynamic, emitting rotational dumbells with liquid lobes linked by thinning saliva threads. We also image high-speed air fronts produced during plosion, with speeds as fast as tens of meters per second, classifying plosive consonant phonation as a violent atomization event like sneezing.

1. Introduction

Airborne aerosols are now recognized to be the most significant transmission route for Severe Acute Respiratory Syndrome CoronaVirus 2 (SARS-CoV-2), responsible for the COVID-19 pandemic (Leung, 2021; Zhang et al., 2020). While coughing and sneezing of symptomatic individuals are evident sources of infected saliva and mucus aerosols (Bourouiba et al., 2014; Duguid, 1946; Johnson et al., 2011; Mittal et al., 2020; Scharfman et al., 2016; Wells, 1934), half of the transmissions actually occur at the presymptomatic or asymptomatic stages during social interactions (Hamner et al., 2020; He et al., 2020; Hijnen et al., 2020; Jang et al., 2020; Lu et al., 2020; Park et al., 2020). Since SARS-CoV-2 replication occurs mostly in the upper oropharyngeal tract (Gandhi et al., 2020; To et al., 2020), saliva atomization via phonation presents a faint but potent conduit for pathogen transmission, potentially promoting global dissemination.

We demonstrated three years ago that phonetic aerodynamic features, such as the plosion of consonants, are tied to both long distance transport of exhaled material (>2 m, Abkarian et al., 2020) and the prominent production of saliva droplets via a complex

---

[*] Corresponding author.
E-mail address: manouk.abkarian@umontpellier.fr (M. Abkarian).
[1] These authors contributed equally.

https://doi.org/10.1016/j.jaerosci.2023.106282
Received 27 July 2023; Received in revised form 2 October 2023; Accepted 4 October 2023

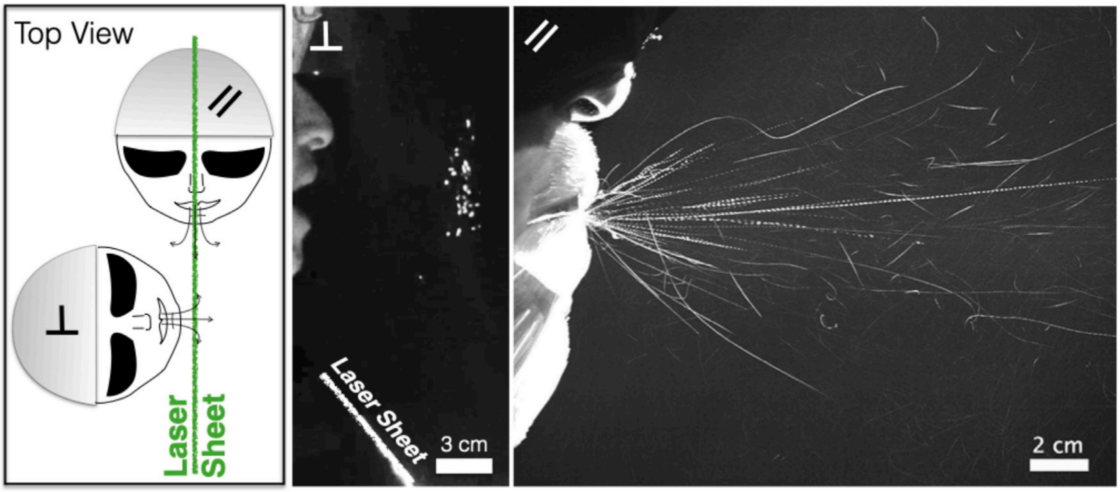

Fig. 1. (Left) Schematic of the two configurations of speech aerosol characterization using a laser sheet. (Middle) The speaker talks orthogonal to the sheet, and the scattered light from the crossing aerosols is captured with a high speed camera for counting droplets. (Right) The speaker pronounced /pa/ in /papa/, with the emitted aerosols propagating parallel to the sheet. The image is a time projection over 100 ms to visualize the trajectories of the droplets leaving the lips.

process of filament stretching and instability at the oral cavity (Abkarian & Stone, 2020) (see an example in Fig. 5A). Constitutive aerosol droplets rapidly evaporate, and their final size depends strongly on their initial size and composition as well as on the environmental conditions (Pöhlker et al., 2021). Yet, quantitative characterization of respiratory aerosol size distributions is difficult to obtain due to their low number density (a few thousand can be spread over volumes ranging from cm^3 to m^3, depending on the distance from the mouth). Their size can range over three decades, from 1 to 10^3 μm, and they are propelled at speeds in excess of ten meters per second (as we show below).

Measuring aerosol droplet production rate and size distribution during speech is crucial to reveal conditions affecting transmission and thus develop effective mitigation strategies, not only for SARS-CoV-2, but also for other airborne viruses (e.g. influenza) and bacterial pathogens (e.g. tuberculosis and meningitis). While multiple studies have measured the number and size of aerosols produced from sneezes and coughs, the range of results differs by orders of magnitude, partly due to the dynamic nature of the aerosol particles, and partly due to the variety of measurement techniques employed, wherein each one covers a small range of particle sizes, and it is often difficult to directly compare results of different techniques (Ai & Melikov, 2018; Duguid, 1946; Pöhlker et al., 2021; Seminara et al., 2020; Xie et al., 2007, 2009; Zhang et al., 2015). For speech aerosols, the relationship between linguistic characteristics and size distribution is still relatively understudied (Asadi et al., 2019, 2020; Duguid, 1946; Johnson et al., 2011; Loudon & Roberts, 1967). Each phonation event produces a few hundreds of aerosol droplets. While the total number is very small compared to a cough or sneeze, the accumulation of these droplets during an indoor conversation becomes significant (Chao et al., 2009; Johnson et al., 2011; Loudon & Roberts, 1967; Morawska et al., 2009; Papineni & Rosenthal, 1997; Pöhlker et al., 2021).

Many current techniques for aerosol sizing necessitate a large distance between the emitter and aerosol sizing instrument, and often this space is perturbed by funnels, tubes, and aspiration (Asadi et al., 2019, 2020; Johnson et al., 2011). The degree to which the results of such techniques are affected by evaporation, condensation, and surface adsorption effects remains unclear (Xie et al., 2007, 2009). An interesting approach used at the beginning of the COVID-19 pandemic was to place a laser light sheet orthogonal to aerosol propagation. The detection of scattered light allowed for droplet counting at a distance of 10–20 cm from the mouth during phonation (Abkarian & Stone, 2020; Anfinrud et al., 2020; Stadnytskyi et al., 2020) (see Fig. 1), thereby evading many of the potential artifacts described above. A complementary implementation projects the laser sheet directly onto the face and parallel to aerosol propagation (also visible in Fig. 1). Although this approach restricts observations to droplets within the plane of the laser sheet, it facilitates particle size determination down to 30 μm using particle tracking velocimetry, via multiple synchronized high-speed cameras and complex 3D localization algorithms (Kim et al., 2022). More recently, the laser sheet approach has been combined with an interferometric characterization to determine droplet size (Grandoni et al., 2023). However, this method is restricted in its temporal resolution, lacks the ability to localize droplets in 3D, and cannot observe formation mechanisms. In fact, laser sheet approaches, though powerful, suffer from three important limitations: They have a narrow focal plane, inherent to the sheet thickness and conventional imaging approaches; it is difficult to quantify the size of the droplets produced in time; and it is not possible to follow atomization dynamics in 3D.

Digital in-line holography (DIH) (Li & Picart, 2013) is uniquely positioned to resolve both the position and morphology of dynamic scattering objects over large 3D volumes. By recording the interference pattern of the incident and scattered light, or hologram, DIH is able to numerically reconstruct the image at chosen focal planes, yielding the 3D positions and full morphology. As numerical reconstructions can be performed offline, DIH is only limited temporally by the acquisition speed of the camera and the amount of light, and it thus presents a very powerful, easy to implement, and robust solution for 3D characterization of dynamical processes. It has been widely employed in the fields of biological, biomedical, and materials science, with applications ranging from

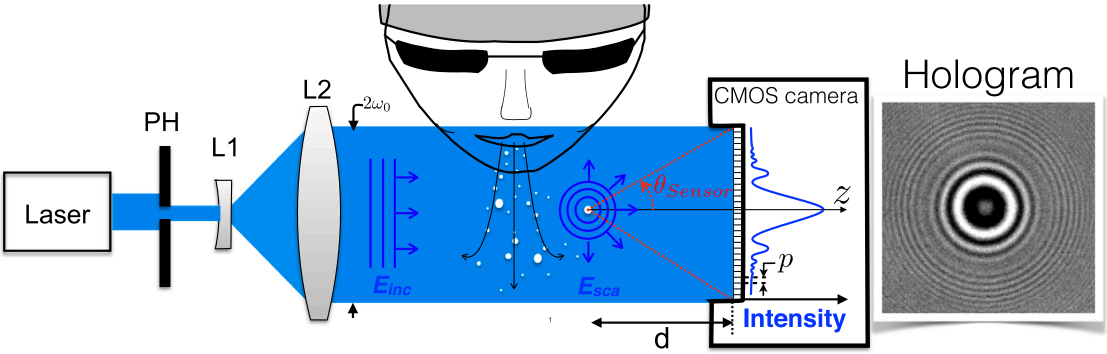

Fig. 2. Schematic of the digital inline holography setup. The laser passed through an aperture pinhole (PH), and was then expanded to a width of $2w_o$ using a Galilean telescope (L1 and L2). The speaker positioned their head adjacent to the laser and spoke orthogonal to the beam propagation direction. The interference pattern was acquired by a CMOS camera of pixel size p at a distance d from the speaker. The hologram (right), acquired onto the CMOS sensor, is the interference pattern between the collimated incident plane wave, E_{inc} and the scattered light from particles, E_{scat}.

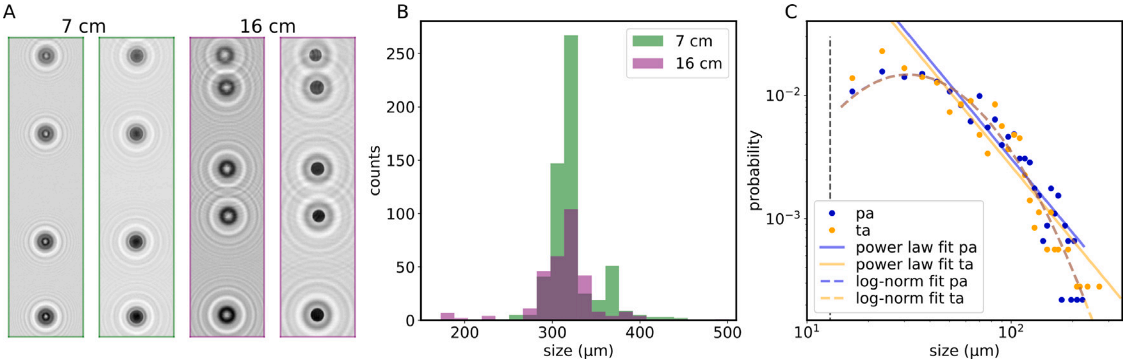

Fig. 3. (A) A chain of falling droplets, imaged at an approximate distance d of 7 cm (green outline) and 16 cm (purple outline). For each distance, the hologram is shown on the left and the projected reconstruction on the right. (B) A histogram of the sizes of the reconstructed droplets for the two distances. The number of droplets measured was 585 and 304 for 7 cm (green) and 16 cm (purple), respectively. (C) A histogram of the reconstructed sizes of respiratory droplets at the exit of the mouth during pronunciation of /pa/ or /ta/. The gray dashed line marks the Nyquist limit, twice the pixel size. The number of droplets measured was 683 and 539 for /pa/ and /ta/, respectively. Solid blue and orange lines show the fit of a Pareto distribution of power 2 to droplets > 50 µm of /pa/ and /ta/, respectively (see Eq. (6), β = 30.7 and 26.8 for /pa/ and /ta/, respectively). Dashed blue and orange lines show the fit of a log-normal distribution to all data points of /pa/ and /ta/, respectively (see Eq. (7), $\hat{\mu}$ = 3.9, $\hat{\sigma}$ = 0.7, β = 0.6 for both /pa/ and /ta/). See Methods for details. (For interpretation of the references to color in this figure legend, the reader is referred to the web version of this article.)

the characterization of cells (Javidi et al., 2021; Memmolo et al., 2014), motile microorganisms (Bedrossian et al., 2017; Thornton et al., 2016; Wang, Garmann et al., 2016), colloids (Altman & Grier, 2020; Wang, Mcgorty et al., 2016), atmospheric aerosols (Berg, 2022), and aerodynamic fragmentation (Essaï di et al., 2021; Guildenbecher et al., 2017).

Here, we demonstrate the power of DIH to quantify the fluid dynamics of speech. With a simple and robust optical setup, we visualize the dynamic formation of filaments and droplets directly at the mouth, quantifying features over two orders of magnitude in size and moving at speeds up to 12 m/s. High-speed imaging, with sub-millisecond and up to 13 µm resolution, reveals the dynamic spatio-temporal evolution of these aerosols in 3D over a large volume of interest.

2. Experiments and results

Holographic imaging of speech droplets and size characterization

We combined high-speed imaging with DIH, and a schematic of the setup is shown in Fig. 2 (with a detailed description in Methods). One of the strengths of our DIH setup is the ability to determine the size of droplets over a large axial range from the camera. We demonstrate this by recording the holograms of a stream of monodisperse droplets produced by an acoustic generator and falling under the force of gravity at a distance of 7 and 16 cm from the camera, as shown in Fig. 3A (see Methods). The distribution of droplet sizes, determined from the numerical reconstructions and shown in Fig. 3B, are independent of the distance from the camera over this range.

We had shown previously with the laser sheet approach that the production rate of speech-induced droplets close to the mouth is dependent upon the spoken linguistic features, though we were ignorant to both the droplet size and their axial trajectories (Abkarian & Stone, 2020). Here, we show that DIH is an excellent approach to image respiratory droplets exhaled at the mouth, near their initial hydration state, and as a function of the pronounced linguistic feature. To do so, the head of a subject was positioned with the lips at the height of and directly adjacent to the beam, such that expelled respiratory filaments and droplets would travel approximately orthogonal to the laser beam. We illustrate the power of this approach by quantifying the distribution of aerosol size from two different stop consonants, /p/ and /t/, both followed by the vowel /a/, when saying either /pa/ or /ta/. For both these plosive consonants, pressure is increased in the oral cavity before sudden release, either by opening the lips in the case of /p/ (also called a bi-labial consonant), or by detaching the flat tongue from the alveolar ridge and upper teeth (also called a denti-alveolar consonant). We imaged tens of utterances of /pa/ and /ta/ from a single speaker. We observed very similar droplet size distributions for the two linguistic features, with a peak near 25 μm (Fig. 3C), potentially suggesting a similarity in the underlying atomization processes associated to filament production and break-up. As seen previously, this data is well fit by a log-normal probability distribution function. Alternatively, the larger droplets (>50 μm) are well fit by a Pareto distribution of power 2 (Balachandar et al., 2020).

Moreover, we note that the lower limit for size quantification is approximately twice the pixel size of the camera. This limit is apparent in the distribution shown in Fig. 3C. In principle, there are two imaging resolutions associated to DIH reconstruction at a distance d (see, for instance, Berg, 2022). One is the image-plane transverse resolution $\delta_t(d)$ and the other is the axial or longitudinal resolution $\delta_l(d)$. Both are given by the Abbe diffraction limit due to the wave nature of light, by $\delta_t = \lambda/(2 \cdot NA)$ and $\delta_l = \lambda/(\sqrt{2} \cdot NA^2)$, where $NA = sin(\theta_{sensor})$ is the numerical aperture of the sensor, associated to the angle θ_{sensor} as noted in Fig. 2. The NA can be expressed as a simple geometric relationship with the distance d between the diffusing element and the surface of the sensor of dimension np (where n is the number of pixels in the radial direction and p is the physical pixel size) as $NA = (np/2)/\sqrt{(np/2)^2 + d^2}$ (Berg, 2022). This leads to:

$$\delta_t(d) = \left(\frac{\lambda d}{np}\right). \quad (1)$$

The typical distance between the droplets and the sensor ranged between 3 and 20 cm. We tested three cameras with sensor sizes ranging from 1.5 cm to 3.5 cm, corresponding to an NA which varies in our experiments from 0.008 to 0.32. For the laser wavelength used, $\delta_t(d)$ ranges between 0.4 to 6.5 μm for the furthest particles, while $\delta_l(d)$ ranges from 3.2 to 626 μm. As expected, longitudinal resolution is at least six times poorer than the transverse, for a given NA, since $\delta_l(d) = \delta_t(d)\frac{\sqrt{2}}{NA}$ and its resolution decreases with distance. Moreover, the low range of the transverse resolution is calculated for an ideal situation where the sensor can capture and resolve all the interference fringes of a given droplet. If the droplets are too far to be resolved, one could, in principle, decrease d to increase resolution, since θ_{sensor} would increase. While this would resolve more interference fringes, there is a strong limit, in practice. Only a given portion of the sensor will be able to resolve fringes due to limited pixel size and sensitivity (dynamical range). In this case, the resolution will only be given by the sampling theorem of Nyquist with $\delta_t \approx 2p$ (Berg, 2022; Guildenbecher et al., 2017). Thus, in reality, we have:

$$\delta_t(d) = max\left[\left(\frac{\lambda d}{Np}\right), 2p\right]. \quad (2)$$

For our purposes, as $2p$ is always greater than Abbe's diffraction limit, we are limited by the pixel size rather than by optical considerations for lens-less systems. It should be noted, however, that the resolution can be increased by two means. First, by using a bi-telecentric magnification system (commonly 2x to 4x) in front of the sensor (Guildenbecher et al., 2017; Spuler & Fugal, 2011), the resolution would increase to around 3-4 μm, though at the detriment of the size of the field of view. Second, a camera with a smaller pixel size could be used. Current lithography technologies allow for pixels down to around two microns in size, which would fix the Nyquist limit to about four microns. However, to maintain the NA, the number of pixels needs to increase accordingly, and a smaller pixel size reduces sensitivity. For these reasons, to date, a large array of small pixels necessitates slower acquisition rates (tens of frames per second). While short exposures can still be obtained by using a pulsed laser (Spuler & Fugal, 2011), thereby yielding a snapshot of aerosol size, such an approach forbids dynamical studies.

The power of DIH to examine the 3D dynamics of speech-induced droplets is demonstrated in Fig. 4. Multiple overlaid projected reconstructions of droplets leaving the mouth are shown in Fig. 4B, and the same droplets are shown in Fig. 4A in a 3D volume, spanning ∼10 cm in axial range. Full 3D localization allows for the correct estimation of speed, and the droplets shown in Fig. 4A are propagating at rates of 1–9 m/s.

Visualizing speech filament formation, whipping and destabilization

Fundamentally, the interference pattern of a hologram contains the full 3D information of the objects which scattered the incident light, an optical principle that won its inventor, Dennis Gabor, the Nobel prize (Gabor, 1948). Thus, each hologram of our movies contains information of the dynamic atomization process occurring at the lips during speech. Previously, we used high-speed standard video imaging to capture the formation of filaments during the initial stage pohlof lip detachment during the pronunciation of /papa/, as shown in Fig. 5A (Abkarian & Stone, 2020). Using a 105 mm macro-objective, we observed the sequential filament formation from the initial stretched film of saliva connecting the lips in the central region of the Cupid's bow. As the lips detach, the film stretches, and a pore is quickly formed, which leads immediately to the first filaments. These filaments are then stretched by the air flow, up to centimeters in arc length, while still attached to the upper and lower lips. As the lips continue to separate,

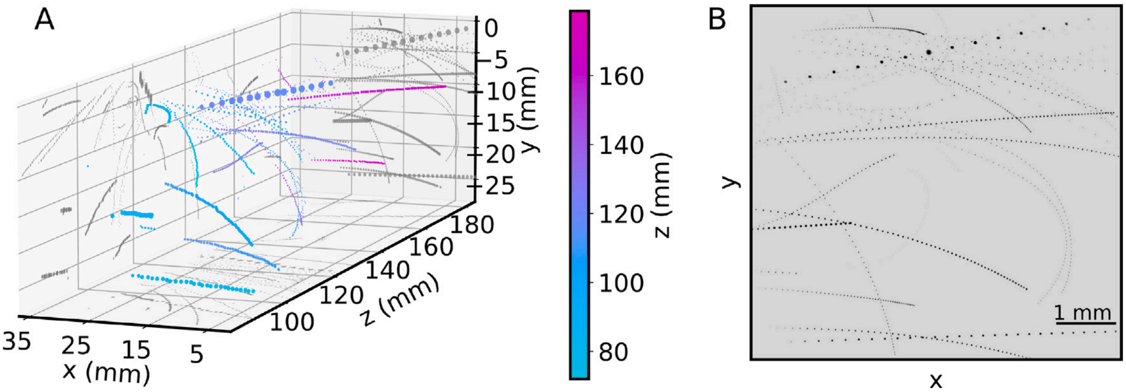

Fig. 4. (A) The 3D localization of droplets, captured within one cm from the exit of the mouth. As the reconstructed and measured size of the droplets is small compared to the detection volume, they are shown here as spheres with a 2000 times magnification factor. The color denotes their position in z. (B) An overlaid sequence of sequential projected reconstructions of the same droplets shown in (A). The mouth, not shown, is on the left. (For interpretation of the references to color in this figure legend, the reader is referred to the web version of this article.)

the new film being formed at the corners of the lips destabilizes, leaving behind new filaments that are subsequently stretched by the air flow. Quantitative measurements of the dynamics of this process were previously limited by the narrow focal plane of the objective and the image resolution of about 50 μm (Abkarian & Stone, 2020). Here, with our DIH setup, we image this process and numerically refocus each individual filament, yielding the 3D localization, size, and trajectory as a function of time over the entire axial range of the lips. Fig. 5B shows a hologram of a fixed instant in time and a projected reconstruction during the pronunciation of /pa/, where multiple filaments in different stages of deformation are seen simultaneously.

The majority of these filaments present a similar temporal evolution. Within a few milliseconds they deform into a catenary shape while thinning in diameter, often close to the Nyquist resolution limit, as small as 13 μm (reachable for one of the cameras used in our DIH setup). Then, we observe one of two different rupture dynamics. In the first, as illustrated in Fig. 5C, the filament is initially attached to the two opening lips (not seen in the figure), while being stretched by the fast air flow from the sudden release of pressure during the pronunciation of the consonant /p/. Then, one extremity ruptures and accelerates faster than the filament body, reaching a speed of ~6.5 m/s in Fig. 5C, whipping the air while thinning. In a second type of destabilization, pictured in Fig. 6A–B, two rupture points occur simultaneously near the attachment bases of the filament to each lip. This releases the filament in its catenary shape, which is convected by the air flow. Again in this case, the extremities travel faster than the body of the filament, leading to a local 'S' shape reconstructed in 3D in Fig. 6A. For both filaments, a peristaltic Rayleigh–Plateau instability propagates from the extremities to the thicker regions. The subsequent thinning produces smaller droplets bound by thin filaments smaller than 10 μm in diameter. Interestingly, the whipping dynamics often shed fast rotating dumbbell-shape droplets with rotation frequencies of several hundreds of Hertz, as visible in Fig. 6C–F. Depending on the initial distance between the two lobes, we observe either breakup of the adjoining filament, often preceded by secondary beads-on-a-string destabilization after thinning (Fig. 6C and E), or a coalescence into a single larger droplet. The latter occurs when the distance between the lobes is of the same order as their size, as previously described for dumbbell shape droplets made of Newtonian fluids (Elkins-Tanton et al., 2003) (Fig. 6F), for which destabilization has been studied (Brown & Scriven, 1997). However, orbiting dynamics such as those shown in Fig. 6F are the result of visco-elastic stabilizing effects that maintain the attached filament for a long period of time compared to the analogous Newtonian situation.

Various applications of digital inline holography

The strength of DIH to yield high speed 3D localization, dynamics, and morphology lends itself to applications beyond speech-induced aerosols, and we demonstrate just a few in Fig. 7. While it is commonly assumed that the droplets emitted during a cough are formed within the airway system (Scharfman et al., 2016), Fig. 7B shows the evolution of a single long filament leaving the mouth during a cough. In Fig. 7A, at the bottom and outside the frame is an arm (a couple hairs from the arm are visible in the lower right). The hologram shows airborne particles which arise upon gentle rubbing of the skin of the arm, shown magnified in Fig. 7C–D. Finally, the sensitivity of this technique is such that the front of exhaled air which proceeds the ejection of filaments can be observed, with simultaneous observation and tracking of filaments and droplet formation, as shown in Fig. 7E (during the phonation of /pa/ in /papa/). In this sequence, the exhaled air is traveling on the order of 12 m/s.

3. Discussion

Unlike sneezing (Scharfman et al., 2016) and coughing, Chao et al. (2009) which produce air flow velocities between 10 and 35 m/s, phonation has been measured to generate flows on the order of only 1 to 4 m/s (Abkarian et al., 2020; Chao et al., 2009;

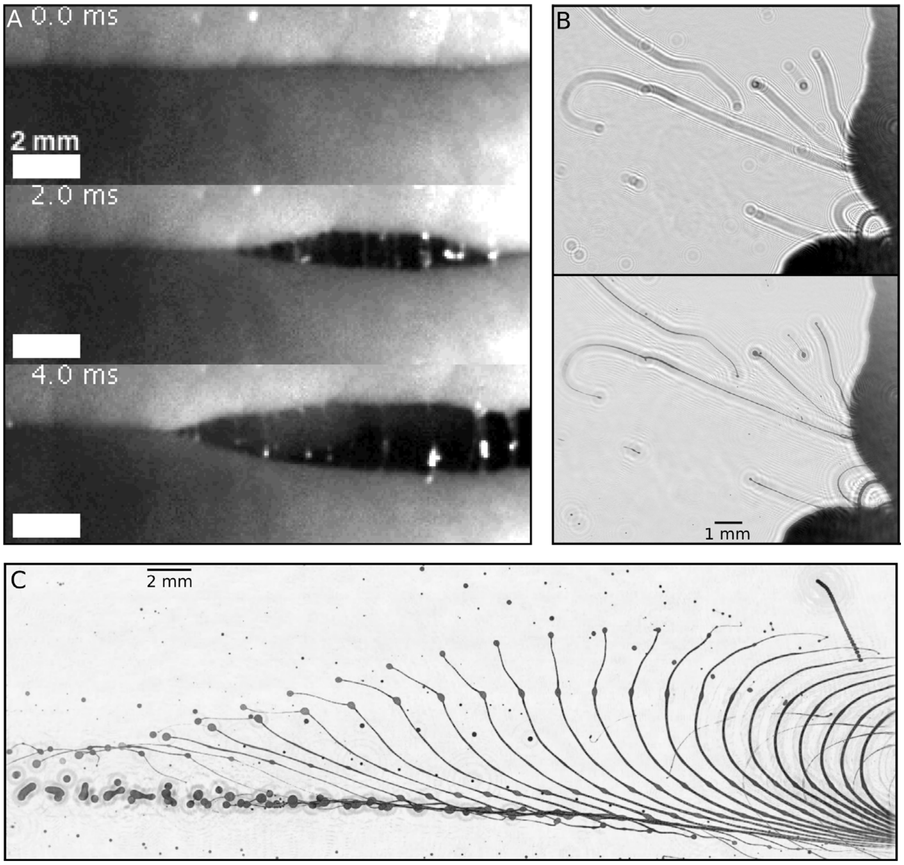

Fig. 5. (A) A sequence of images from a high speed camera as a speaker pronounces /pa/. From top to bottom, pressing the lips together spreads a microscopic salivary lubrication layer, which forms vertical thin filaments within a few ms as the lips separate. Images from Abkarian and Stone (2020). (B) A single raw hologram (top) and its projected reconstruction (bottom) of filaments forming at the lips and breaking during the pronunciation of 'pa'. (C) An overlaid sequence in time of multiple projected reconstruction frames of a filament as it leaves the mouth (on the right, not shown).

Grandoni et al., 2023, 2023; Kim et al., 2022). However, our high-speed DIH approach, performed directly at the mouth, shows that the very initial stage of filament extension, especially in the case of plosive consonants, produces expired air flows up to 10–20 m/s, depending on the voicing features and intensity (see for example Fig. 7E with 12 m/s measured for the bilabial plosive consonant /p/). This places plosive consonant pronunciation closer to a violent atomization process.

In sneezing (Scharfman et al., 2016), atomization is described by mucosalivary fluid sheets that puncture, retract into millimeter-scale ligaments, then further stretch and ultimately break into droplets. This fragmentation sequence has been recently simulated for Newtonian fluids (Kant et al., 2023). In comparison, atomization due to plosive consonant phonation is a process involving the formation of thin films attached to fast opening surfaces provided by the lips (for /p/ or /b/) or the tongue and teeth (for /d/ or /t/). Pores nucleate and propagate in a few milliseconds, producing thin filaments on the order of hundred of microns connecting the moving surfaces (Fig. 5). The airflow then induces the large scale deformation and thinning of the filaments to thicknesses as small as 13 μm and thinner, as seen in Figs. 5 and 6. The presence of the fast moving surfaces anchors the films and filaments and dictates the destabilization sequence which, while the full details remain to be understood, ultimately determines the final droplet size distributions (Fig. 4). Moreover, the beads-on-a-string instability that we observe for the thinnest filaments is a sign of a strong visco-elastic component in these flows. This same effect prevents rotating dumbbell shaped droplets (Fig. 6) from breaking, and allows the adjoining filaments to thin to dimensions smaller than 10 μm. Final droplet size can then easily reach the critical 60 μm limit (Netz & Eaton, 2020), where an aerosol droplet becomes susceptible to large scale transport, due to rapid evaporation that reduces its size and thus sedimentation rate, promoting airborne transport via ambient air flow (Pöhlker et al., 2021).

4. Conclusions

Our simple DIH setup and reconstruction methods allow for the measurement of the full dynamics of the stretching and breaking of saliva filaments in 3D, allowing us to probe the mechanisms of aerodynamic fluid fragmentation and aerosolization within the oral cavity. Such dynamics remain poorly understood for violent expirations such as coughs and sneezes (Scharfman et al., 2016), and

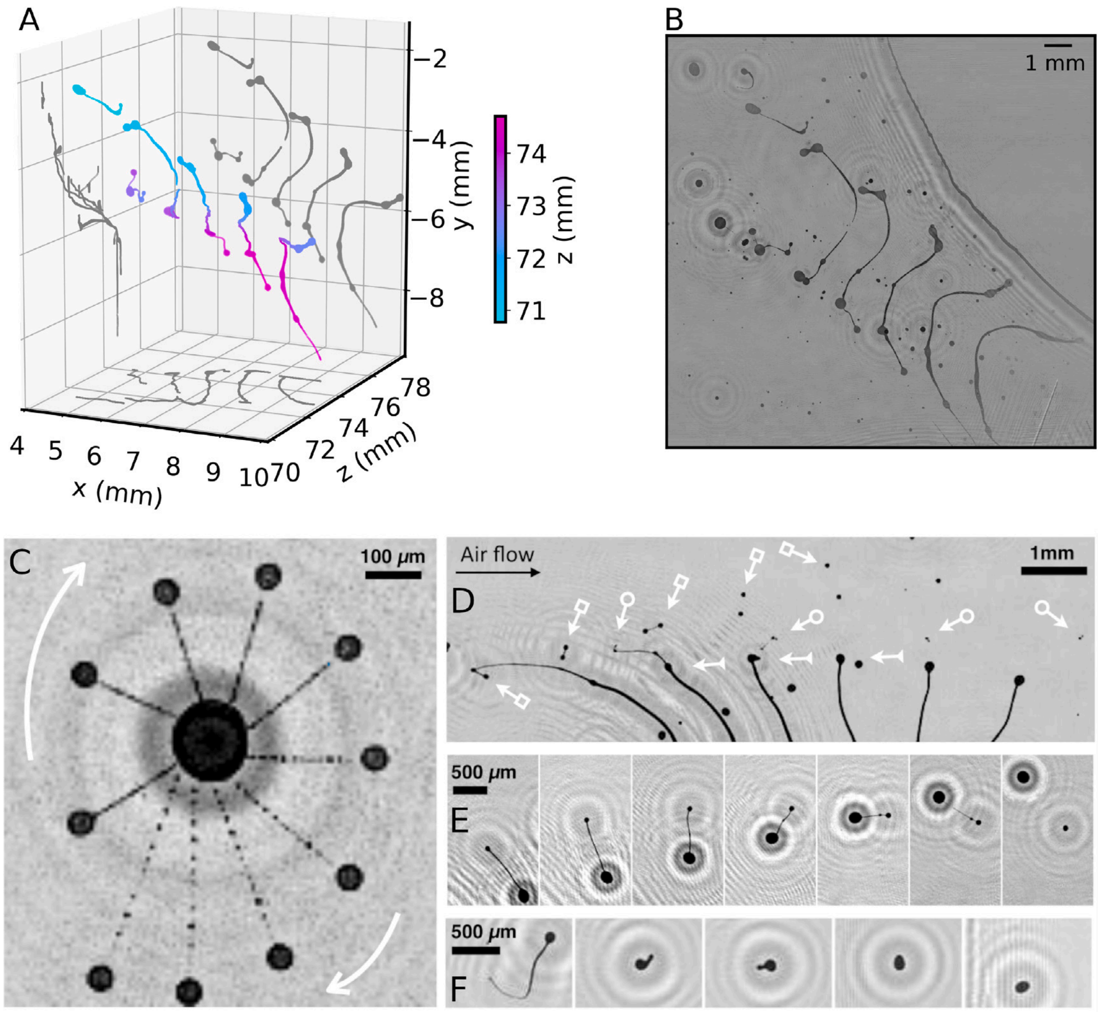

Fig. 6. (A) A 3D plot of the evolution of a filament as it leaves the mouth, where the color denotes the position in z. (B) An overlaid sequence of sequential projected reconstructions of the filament shown in (A) (the mouth is on the bottom right, not shown). (C–E) Rich dynamics of 'dumbbells' or orbiting droplets. (C) Ten sequential projected reconstructions, each 0.42 ms apart, aligned by the center of mass of the central droplet and superimposed, showing orbiting droplets as the filament which connects them elongates and demonstrates the 'beads on a string' phenomenon (D) Six projected reconstructions superimposed (air flow from left to right, as shown by the black arrow), each 0.21 ms apart, showing a filament which has just broken from the lips at one end and whips outward, releasing a droplet pair, which orbits for two frames before the connecting filament ruptures (arrows with open square). A second pair of orbiting droplets is released one frame later, and this pair nearly coalesces two frames later (arrows with open circle). A third pair remains connected to the original filament, coalescing within two frames (arrows with closed triangle). (E) Seven projected reconstructions, each 0.21 ms apart and with a fixed frame of reference, showing a droplet pair whose connecting filament breaks. (F) Five projected reconstructions, each 0.21 ms apart and with a moving frame of reference, showing a droplet pair which quickly coalesces. (For interpretation of the references to color in this figure legend, the reader is referred to the web version of this article.)

are almost entirely unexplored for speech. The complex fragmentation dynamics are governed by the evolving physico-chemical properties of saliva and hydrodynamic instability mechanisms, such as the Rayleigh–Plateau, Kelvin–Helmholtz, and Rayleigh–Taylor instabilities (Sattler et al., 2012; Vadivukkarasan, 2021). Reliable quantification of the sizes and velocities of nascent and evolving aerosol droplets will enable an understanding of the interplay between saliva's rheological properties and the modes of these instabilities. Quantitative characterization of speech-induced saliva aerosolization is vital to modeling and understanding respiratory pathogen transmission and the subsequent development of informed public health policies. Digital inline holography presents a promising tool in this regard.

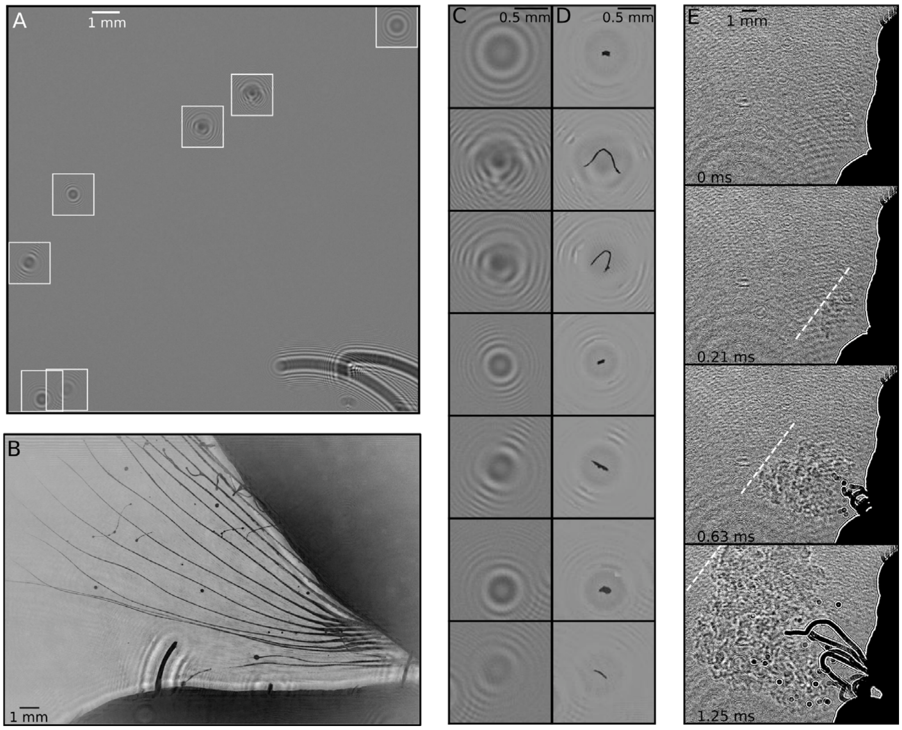

Fig. 7. (A) An image from a video recorded near the arm (arm hair visible in lower right corner), while the skin was lightly rubbed. The white boxes are magnified and shown in (C–D). (B) An overlay of 13 sequential reconstructions showing a long filament leaving the mouth during a cough. (C) the raw holograms and (D) the projected reconstructions of the boxed regions of (A). (E) Sequential holograms showing the exhaled air leaving the mouth (on the right) during the pronunciation of /pa/, prior to the appearance of respiratory filaments and particles. The front of the exhaled air is marked with a white dotted line to aid the eye.

5. Methods

Digital in-line lens-less holography setup

A schematic of the combined high-speed imaging with DIH setup is shown in Fig. 2. A 488 nm laser diode (Coherent Obis LX/LS, operating at 40–140 mW) was passed through an aperture (Thorlabs, 50 μm pinhole) and expanded to give a beam diameter of ~30 mm. We note that spatial filtering of the laser with an objective and smaller pinhole could improve the hologram resolution in a future implementation of this setup. The chain of falling droplets shown in Fig. 3 was generated by the Monosize Droplet Generator (MDG, Model: TSI MDG100). The MDG produces a stream of uniform size drops in the range of 50 μm to 300 μm.

To image respiratory aerosols, the head of the subject was positioned with the lips at the height of and directly adjacent to or within the collimated beam, facing perpendicular to the direction of laser propagation, such that expelled respiratory filaments and droplets would travel approximately orthogonal to the laser beam. This allowed for the full visualization of the formation of saliva filaments between the lips, followed by their extension and eventual fragmentation into droplets. We also visualized the direct ejection of droplets from deeper inside the oral cavity. The distance between the lips and the camera sensor ranged from 3–20 cm. Appropriate laser safety glasses were worn by subjects during experiments.

Interference patterns were recorded onto one of three different CMOS cameras (Photron Fastcam NOVA R5, ROI: 2048 × 1472 pixels, pixel size of 6.5 μm, Phantom VEO 1310, ROI: 1280 × 960 pixels, pixel size of 18 μm, Phantom v2640, ROI: 2048 × 1942 pixels, pixel size of 13.5 μm) at a framerate of 4000–5000 frames per second and an exposure time of 2 μs. From the recorded holograms, we create 'projected reconstructions', wherein each portion of the multiple filaments and droplets within the recorded 3D volume is numerically reconstructed and represented in its own focal plane, effectively projecting a 3D volume into a single focal plane (see below for details).

Numerical reconstructions of holograms

Angular spectrum hologram reconstruction is a digital holography technique that reconstructs a hologram by performing a 2D discrete Fourier transform on the hologram and multiplying it by a phase factor, which depends on the axial propagation distance and angle of incidence of the object wave (see Li and Picart (2013) for details). The resulting complex wavefront is then subjected to

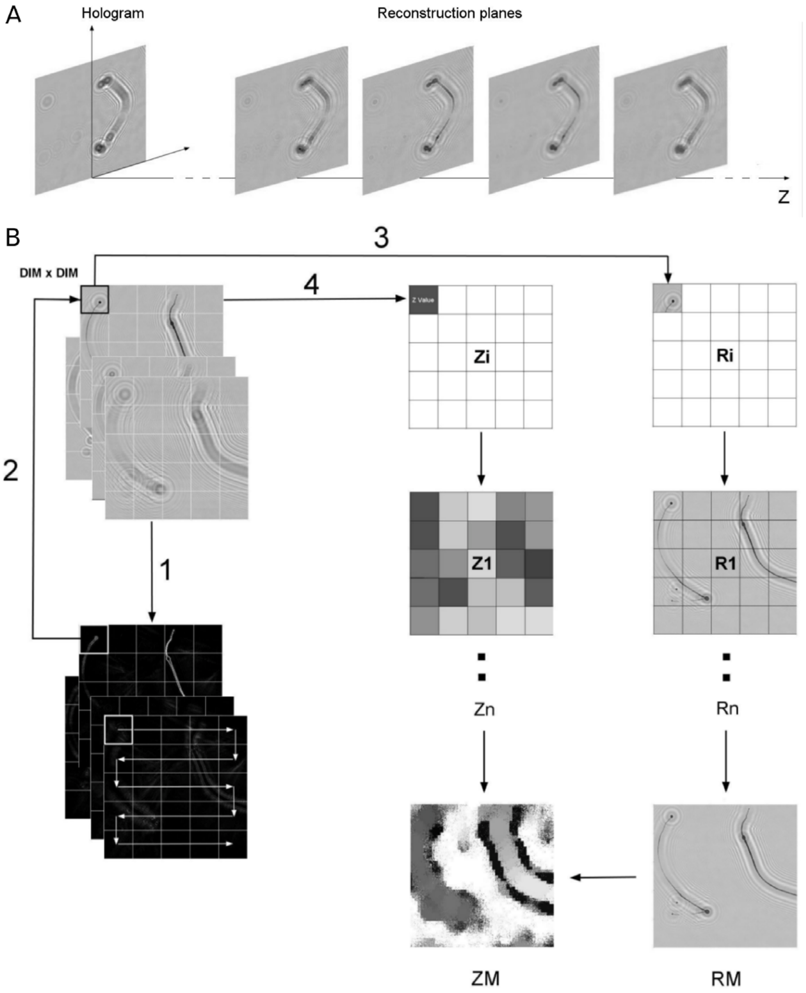

Fig. 8. (A) A schematic depicting the angular spectrum reconstruction method. The recorded hologram, $I(x,y)$ is shown on the left, and multiple reconstructed images at increasing axial distance are shown on the right. (B) A schematic depicting the creation of the projected reconstructions, as described in the Methods. Briefly, step 1 calculates the magnitude of the image gradient for the sequence of reconstructed images at various axial propagation distances. Considering an ROI of dimension $D \times D$ pixels, the variance of the pixel values of the gradient image is used to choose the ideal axial position for the ROI, depicted in step 2. Steps 3 and 4 build the intermediate image, Ri, and the intermediate map of axial position, Zi. By translating the ROI, steps 2–4 are reiterated to build $R1$ and $Z1$. The initial origin of the ROI is shifted and the entire process repeated to finally arrive at R_M and Z_M.

an inverse Fourier transform to obtain the reconstructed image. Given a recorded hologram $I(x,y)$, the reconstructed image $R_z(x,y)$, for a certain axial distance z, was calculated as,

$$R_z(x,y;z) = \mathcal{F}^{-1}\left[\mathcal{F}\left[I(x,y)\right]H_z(u,v)\right] \tag{3}$$

$$H_z(u,v) = exp\left(\frac{-2\pi i z}{\lambda}\sqrt{1-(\lambda u)^2-(\lambda v)^2}\right) \tag{4}$$

$$\sqrt{(u^2+v^2)} \leq \frac{1}{\lambda} \tag{5}$$

where $H_z(u,v)$ is the angular spectrum transfer function, (u,v) denotes the corresponding Fourier frequencies of (x,y), λ denotes the wavelength of illumination light, and $\mathcal{F}$ and $\mathcal{F}^{-1}$ are the Fourier transform and inverse Fourier transform, respectively. Fig. 8A shows an example hologram and multiple reconstructed images at different axial distances. It should be noted that, for reasons of symmetry, there are always two images appearing in the reconstruction of a hologram, and the unwanted, out of focus twin-image fringes can sometimes obscure the object of interest. While not used in this work, universal iterative approaches of reconstruction can be implemented, with no assumptions about absorbing or phase shifting properties of the object, to retrieve both amplitude and phase distributions (Latychevskaia & Fink, 2007)

Projected reconstructions

In order to visualize the formation and evolution of filaments and droplets in a 3D volume, we create projected reconstructions which numerically re-focus each portion of a hologram $I(x,y)$, effectively collapsing a 3D volume onto a single, focused z plane.

For a given hologram $I(x,y)$, we use the angular spectrum method described above to calculate the reconstructed images $R_z(x,y)$ for a sequence of axial propagation distances $\{z_1, z_2, \ldots, z_p\}$, yielding $\{R_{z_1}(x,y), R_{z_2}(x,y), \ldots, R_{z_p}(x,y)\}$. For each reconstructed image, we calculate the magnitude of the image gradient, yielding $\{G_{z_1}(x,y), G_{z_2}(x,y), \ldots, G_{z_p}(x,y)\}$ (step 1 in Fig. 8B). Considering a region of interest (ROI) of dimension $D \times D$ pixels, placed originally at $(x,y) = (0,0)$, we calculate the variance of the pixel values in the ROI for each magnitude image. The highest variance corresponds to the ideal (most focused) axial position for that ROI. The image portion of the ROI at the ideal axial position (step 2 in Fig. 8B) is then used to build intermediate image Ri (step 3 in Fig. 8B), and the corresponding z plane populates the intermediate map of axial position, Zi (step 4 of Fig. 8B). Steps 2–4 are reiterated by translating the ROI along $I(x,y)$, to build the image $R1$ and axial map $Z1$.

The origin of the mask is then shifted by dx and dy (where $dx < D$, $dy < D$) and steps 1 to 4 are repeated to construct images $[R_2, \ldots, R_n]$ and axial maps $[Z_2, \ldots, Z_n]$. Then, for each pixel, the median intensity value of that pixel in $[R_1, \ldots, R_n]$, is calculated to give this pixel's value in the final reconstructed image, R_M. The corresponding z value (obtained from the position of the median value in the planes $[R_1, \ldots, R_n]$) is duplicated into the final map of the reconstructed axial distance, Z_M. All projected and numerical reconstructions were performed with homemade C++ software. Typical values for D and (dx, dy) were 40 pixels and 8 pixels, respectively.

Droplet size distribution

The distribution of the reconstructed sizes of respiratory droplets shown in Fig. 3C was fit with a Pareto distribution of power 2,

$$N(s) = \frac{\beta}{s^2}, \tag{6}$$

where $N(s)$ is the size distribution of droplets, s is the droplet size, and β is a normalization constant. The distribution was also fit to a Log-Normal distribution,

$$N(s) = \frac{\beta}{s} \exp\left(\frac{-(\ln s - \hat{\mu})^2}{2\hat{\sigma}^2}\right), \tag{7}$$

where β is a normalization constant, $\hat{\mu}$ is the geometric mean, and $\hat{\sigma}$ is the geometric standard deviation. Non-linear least squares fits were performed using Python's scipy.optimize.curve_fit package.

CRediT authorship contribution statement

Ashley L. Nord: Conceived of and performed the experiments, Drafting of this manuscript. **Patrice Dosset:** Performed all holograph reconstructions and analysis, Drafting of this manuscript. **Pierre Slangen:** Performed preliminary experiments, Drafting of this manuscript. **Manouk Abkarian:** Conceived of and performed the experiments, Drafting of this manuscript.

Declaration of competing interest

The authors have no competing interests to declare that are relevant to the content of this article.

Data availability

Data will be made available on request.

Acknowledgments

We thank Zacaria Essaidi for fruitful discussions of in-line holography and Francesco Pedaci for insightful comments on this manuscript. We thank Patrick Nepveu from VM2 for the loan of a Photron FASTCAM NOVA 4K R5 camera, as well as Constant Taindjis from Ametek France for the loan of a Phantom V2640 camera from Vision Research. We thank Christian Ligoure from Laboratoire Charles Coulomb for the loan of a Phantom VEO 1310 camera from Vision research as well as the TSI droplet generator.

Funding

This research has been supported by the French National Research Agency (ANR), grants ANR-22-CE30-0034 and ANR-21-CO15-0004, as well as by the LabEx NUMEV (ANR-10-LABX-0020) within the I-Site MUSE (ANR-16-IDEX-0006). The CBS is a member of the France-BioImaging (FBI) and the French Infrastructure for Integrated Structural Biology (FRISBI), 2 national infrastructures supported by the French National Research Agency (ANR-10-INBS-04-01 and ANR-10-INBS-05, respectively).

References

Abkarian, M., Mendez, S., Xue, N., Yang, F., & Stone, H. (2020). Speech can produce jet-like transport relevant to asymptomatic spreading of virus. *Proceedings of the National Academy of Sciences of the United States of America*, *117*, 25237–25245.

Abkarian, M., & Stone, H. A. (2020). Stretching and break-up of saliva filaments during speech: A route for pathogen aerosolization and its potential mitigation. *Physical Review Fluids*, *5*, Article 102301.

Ai, Z. T., & Melikov, A. K. (2018). Airborne spread of expiratory droplet nuclei between the occupants of indoor environments: A review. *Indoor Air*, *28*(4), 500–524.

Altman, L. E., & Grier, D. G. (2020). CATCH: Characterizing and tracking colloids holographically using deep neural networks. *The Journal of Physical Chemistry B*, *124*(9), 1602–1610.

Anfinrud, P., Stadnytskyi, V., Bax, C., Bax, A., & Stadnytskyi, V. (2020). Visualizing speech generated oral fluid droplets with laser light scattering. *The New England Journal of Medicine*, *382*(21), 2061–2063.

Asadi, S., Wexler, A. S., Cappa, C. D., Barreda, S., Bouvier, N. M., & Ristenpart, W. D. (2019). Aerosol emission and superemission during human speech increase with voice loudness. *Scientific Reports*, *9*(11), 2348.

Asadi, S., Wexler, A. S., Cappa, C. D., Barreda, S., Bouvier, N. M., & Ristenpart, W. D. (2020). Effect of voicing and articulation manner on aerosol particle emission during human speech. *PLoS One*, *15*(1), Article e0227699.

Balachandar, S., Zaleski, S., Soldati, A., Ahmadi, G., & Bourouiba, L. (2020). Host-to-host airborne transmission as a multiphase flow problem for science-based social distance guidelines. *International Journal of Multiphase Flow*, *132*, Article 103439.

Bedrossian, M., Lindensmith, C., & Nadeau, J. L. (2017). Digital holographic microscopy, a method for detection of microorganisms in plume samples from enceladus and other icy worlds. *Astrobiology*, *17*, 913–925.

Berg, M. J. (2022). Tutorial: Aerosol characterization with digital in-line holography. *Journal of Aerosol Science*, *165*, Article 106023.

Bourouiba, L., Dehandschoewercker, E., & Bush, J. (2014). Violent expiratory events: on coughing and sneezing. *Journal of Fluid Mechanics*, *745*, 537–563.

Brown, R., & Scriven, L. (1997). The shape and stability of rotating liquid drops. *Proceedings of The Royal Society of London. Series A. Mathematical, Physical and Engineering Sciences*, *371*, 331–357.

Chao, C. Y. H., Wan, M. P., Morawska, L., Johnson, G. R., Ristovski, Z. D., Hargreaves, M., Mengersen, K., Corbett, S., Li, Y., Xie, X., & Katoshevski, D. (2009). Characterization of expiration air jets and droplet size distributions immediately at the mouth opening. *Journal of Aerosol Science*, *40*, 122–133.

Duguid, J. P. (1946). The size and the duration of air-carriage of respiratory droplets and droplet-nuclei. *Journal of Hygiene*, *44*(6), 471–479.

Elkins-Tanton, L., Aussillous, P., Bico, J., Quéré, D., & Bush, J. (2003). A laboratory model of splash-form tektites. *Meteoritics & Planetary Science*, *38*, 1331–1340.

Essaï di, Z., Lauret, P., Heymes, F., Aprin, L., & Slangen, P. (2021). Aerodynamic fragmentation of water, ethanol and polyethylene glycol droplets investigated by high-speed in-line digital holography. *Optical Materials*, *122*, Article 111747.

Gabor, D. (1948). A new microscopic principle. *Nature*, *161*, 777–778.

Gandhi, M., Yokoe, D., & Havlir, D. (2020). Asymptomatic transmission, the achilles' heel of current strategies to control Covid-19. *The New England Journal of Medicine*, *382*(22), 2158–2160.

Grandoni, L., Méès, L., Grosjean, N., Leuzzi, G., Monti, P., Pelliccioni, A., & Salizzoni, P. (2023). Interferometric laser imaging for respiratory droplets sizing. *Experiments in Fluids*, *64:80*(4), 1–16.

Guildenbecher, D. R., Gao, J., Chen, J., & Sojka, P. E. (2017). Characterization of drop aerodynamic fragmentation in the bag and sheet-thinning regimes by crossed-beam, two-view, digital in-line holography. *International Journal of Multiphase Flow*, *94*, 107–122.

Hamner, L., Dubbel, P., Capron, I., Ross, A., Jordan, A., Lee, J., Lynn, J., Ball, A., Narwal, S., Russell, S., Patrick, D., & Leibrand, H. (2020). High SARS-CoV-2 attack rate following exposure at a choir practice-skagit county. *Morbidity and Mortality Weekly Report*, *69*(19), 606–610.

He, X., Lau, E., Wu, P., Deng, X., Wang, J., Hao, X., Lau, Y., Wong, J., Guan, Y., Tan, X., Mo, X., Chen, Y., Liao, B., Chen, W., Hu, F., Zhang, Q., Zhong, M., Wu, Y., Zhao, L., ... Leung, G. (2020). Temporal dynamics in viral shedding and transmissibility of COVID-19. *Nature Medicine*, *26*(5), 672–675.

Hijnen, D., Marzano, A., Eyerich, K., GeurtsvanKessel, C., Giménez-Arnau, A., Joly, P., Vestergaard, C., Sticherling, M., & Schmidt, E. (2020). SARS-CoV-2 transmission from presymptomatic meeting attendee, Germany. *Emerging Infectious Diseases*, *26*(8), 1935–1937.

Jang, S., Han, S., & Rhee, J. (2020). Cluster of coronavirus disease associated with fitness dance classes. *Emerging Infectious Diseases*, *26*(8), 1917–1920.

Javidi, B., Carnicer, A., Anand, A., Barbastathis, G., Chen, W., Ferraro, P., Goodman, J. W., Horisaki, R., Khare, K., Kujawinska, M., Leitgeb, R. A., Marquet, P., Nomura, T., Ozcan, A., Park, Y., Pedrini, G., Picart, P., Rosen, J., Saavedra, G., ... Yamaguchi, M. (2021). Roadmap on digital holography. *Optics Express*, *29*(22), 35078–35118.

Johnson, G. R., Morawska, L., Ristovski, Z. D., Hargreaves, M., Mengersen, K., Chao, C. Y. H., Wan, M. P., Li, Y., Xie, X., Katoshevski, D., & Corbett, S. (2011). Modality of human expired aerosol size distributions. *Journal of Aerosol Science*, *42*(12), 839–851.

Kant, P., Pairetti, C., Saade, Y., Popinet, S., Zaleski, S., & Lohse, D. (2023). Bag-mediated film atomization in a cough machine. *Physical Review Fluids*, *8*, Article 074802.

Kim, J., Ouyang, W., Hwang, H., Jeong, H., Kang, S., Bose, S., Kwak, S., Ni, X., Kim, H., Park, J., Chen, H., Soetikno, A., Kim, J., Xu, S., Chamorro, L., & Rogers, J. (2022). Dynamics of plosive consonants via imaging, computations, and soft electronics. *Proceedings of the National Academy of Sciences of the United States of America*, *119*(46), Article e2214164119.

Latychevskaia, T., & Fink, H.-W. (2007). Solution to the twin image problem in holography. *Physical Review Letters*, *98*, Article 233901.

Leung, N. (2021). Transmissibility and transmission of respiratory viruses. *Nature Reviews Microbiology*, *19*, 528–545.

Li, J.-C., & Picart, P. (2013). *Digital holography* (pp. 115–164). John Wiley & Sons.

Loudon, R. G., & Roberts, R. M. (1967). Droplet expulsion from the respiratory tract. *American Review of Respiratory Disease*, *95*(3), 435–442.

Lu, J., Gu, J., Li, K., Xu, C., Su, W., Lai, Z., Zhou, D., Yu, C., Xu, B., & Yang, Z. (2020). COVID-19 outbreak associated with air conditioning in restaurant. *Emerging Infectious Diseases*, *26*(7), 1628–1631.

Memmolo, P., Miccio, L., Merola, F., Gennari, O., Netti, P., & Ferraro, P. (2014). 3D morphometry of red blood cells by digital holography. *Cytometry A*, *85*.

Mittal, R., Ni, R., & Seo, J.-H. (2020). The flow physics of COVID-19. *Journal of Fluid Mechanics*, *894*, F2.

Morawska, L., Johnson, G. R., Ristovski, Z. D., Hargreaves, M., Mengersen, K., Corbett, S., Chao, C. Y. H., Li, Y., & Katoshevski, D. (2009). Size distribution and sites of origin of droplets expelled from the human respiratory tract during expiratory activities. *Journal of Aerosol Science*, *40*(3), 256–269.

Netz, R., & Eaton, W. (2020). Physics of virus transmission by speaking droplets. *Proceedings of the National Academy of Sciences of the United States of America*, *117*, 25209–25211.

Papineni, R. S., & Rosenthal, F. S. (1997). The size distribution of droplets in the exhaled breath of healthy human subjects. *Journal of Aerosol Medicine*, *10*(2), 105–116.

Park, S., Kim, Y.-M., Yi, S., Lee, S., Na, B.-J., Kim, C., Kim, J.-I., Kim, H., Kim, Y., Park, Y., Huh, I., Kim, H., Yoon, H., Jang, H., Kim, K., Chang, Y., Kim, I., Lee, H., Gwack, J., ... Jeong, E. (2020). Coronavirus disease outbreak in call center. *Emerging Infectious Diseases*, *26*(8), 1666–1670.

Pöhlker, M. L., Krüger, O. O., Förster, J.-D., Berkemeier, T., Elbert, W., Fröhlich-Nowoisky, J., Pöschl, U., Pöhlker, C., Bagheri, G., Bodenschatz, E., Huffman, J. A., Scheithauer, S., & Mikhailov, E. (2021). Respiratory aerosols and droplets in the transmission of infectious diseases. (arXiv:2103.01188).

Sattler, R., Gier, S., Eggers, J., & Wagner, C. (2012). The final stages of capillary break-up of polymer solutions. *Physics of Fluids*, *24*(2), Article 023101.

Scharfman, B., Techet, A., Bush, J., & Bourouiba, L. (2016). Visualization of sneeze ejecta: steps of fluid fragmentation leading to respiratory droplets. *Experiments in Fluids*, *57*(24), 1–9.

Seminara, G., Carli, B., Forni, G., Fuzzi, S., Mazzino, A., & Rinaldo, A. (2020). Biological fluid dynamics of airborne COVID-19 infection. *Rendiconti Lincei. Scienze Fisiche e Naturali*, *31*(3), 505–537.

Spuler, S., & Fugal, J. (2011). Design of an in-line, digital holographic imaging system for airborne measurement of clouds. *Applied Optics*, *50*, 1405–1412.

Stadnytskyi, V., Bax, C., Bax, A., & Anfinrud, P. (2020). The airborne lifetime of small speech droplets and their potential importance in SARS-CoV-2 transmission. *Proceedings of the National Academy of Sciences of the United States of America*, *117*(22), 11875–11877.

Thornton, K. L., Findlay, R. C., Walrad, P. B., & Wilson, L. G. (2016). Investigating the swimming of microbial pathogens using digital holography. *Advances in Experimental Medicine and Biology*, *915*, 17–32.

To, K., Tsang, O., Leung, W., Tam, A., Wu, T., Lung, D., Yip, C., Cai, J., Chan, J., Chik, T., Lau, D., Choi, C., Chen, L., Chan, W., Chan, K., Ip, J., Ng, A., Poon, R., Luo, C., ... Yuen, K. (2020). Temporal profiles of viral load in posterior oropharyngeal saliva samples and serum antibody responses during infection by SARS-CoV-2: an observational cohort study. *The Lancet Infectious Diseases*, *20*(5), 565–574.

Vadivukkarasan, M. (2021). A note on the stability characteristics of the respiratory events. *European Journal Mechanics B/Fluids*, *89*, 15–20.

Wang, A., Garmann, R. F., Manoharan, V. N., & vadiv (2016). Tracking E.coli runs and tumbles with scattering solutions and digital holographic microscopy. *Optics Express*, *24*(21), 23719–23725.

Wang, A., Mcgorty, R., Kaz, D., & Manoharan, V. (2016). Contact-line pinning controls how quickly colloidal particles equilibrate with liquid interfaces. *Soft Mater*, *12*.

Wells, W. F. (1934). On air-borne infection: Study II. Droplets and droplet nuclei. *American Journal of Epidemiology*, *20*(3), 611–618.

Xie, X., Li, Y., Chwang, A. T. Y., Ho, P. L., & Seto, W. H. (2007). How far droplets can move in indoor environments–revisiting the wells evaporation-falling curve. *Indoor Air*, *17*(3), 211–225.

Xie, X., Li, Y., Sun, H., & Liu, L. (2009). Exhaled droplets due to talking and coughing. *Journal of the Royal Society Interface*, S703–S714.

Zhang, H., Li, D., Xie, L., & Xiao, Y. (2015). Documentary research of human respiratory droplet characteristics. *Procedia Engineering*, *121*, 1365–1374.

Zhang, R., Li, Y., Zhang, A., & Molina, M. (2020). Documentary research of human respiratory droplet characteristics. *Proceedings of the National Academy of Sciences of the United States of America*, *117*(26), 14857–14863.